GOETHE UNIVERSITÄT FRANKFURT AM MAIN

Fachbereich 13 Physik
Institut für theoretische Physik,
Goethe Universität Frankfurt am Main

Bachelor Thesis

Investigation of the structure of hybrid static potential flux tubes

Lasse Müller

Frankfurt am Main
23. März 2018

Advisor and first supervisor:
Prof. Dr. Marc Wagner
Institut für theoretische Physik
Johann Wolfgang von Goethe Universität Frankfurt am Main

Second supervisor:
Prof. Dr. Owe Philipsen
Institut für theoretische Physik
Johann Wolfgang von Goethe Universität Frankfurt am Main

Selbstständigkeitserklärung

Hiermit erkläre ich, dass ich die Arbeit selbstständig und ohne Benutzung anderer als der angegebenen Quellen und Hilfsmittel verfasst habe. Alle Stellen der Arbeit, die wörtlich oder sinngemäß aus Veröffentlichungen oder aus anderen fremden Texten entnommen wurden, sind von mir als solche kenntlich gemacht worden. Ferner erkläre ich, dass die Arbeit nicht - auch nicht auszugsweise - für eine andere Prüfung verwendet wurde.

Ort, Datum: _____

Unterschrift: _____ (Lasse Müller)

Abstract

In this work the structure of hybrid static potential flux tubes is investigated. First of all a trial state of static quark and antiquark is considered to measure the square of the gluon field components of the ordinary static potential. This is done by evaluating Wilson loops and plaquettes on the lattice. Then the spatial part of these Wilson loops are modified with respect to the quantum numbers of the hybrid state Π_u via 'insertions' off the separation axis of the quark-antiquark pair. For both cases we take a look at the time evolution to confirm convergence. The chromoelectric and chromomagnetic field components are computed on the separation axis and on orthogonal axes in the middle between quark and antiquark. Additionally we obtained results for the hybrid static potential field strength on the plane along the separation axis and an orthogonal one. Those give a complete picture of the gluonic distribution between the colour charges.

Zusammenfassung

In dieser Arbeit wird die Struktur von Flussschläuchen des hybriden statischen Potentials untersucht. Zunächst wird ein Testzustand in Form eines statischen Quarks und Antiquarks betrachtet, um das Quadrat der Komponenten der Farbfelder des gewöhnlichen statischen Potentials zu messen. Dies geschieht durch Berechnung von Wilson Loops und Plaketten auf dem Gitter. Dann wird der räumliche Teil dieser Wilson Loops in Hinblick auf die Quantenzahlen des hybriden Zustandes Π_u mithilfe von 'insertions', welche sich nicht auf der Separationsachse des Quark-Antiquark-Paares befinden, modifiziert. Für beide Fälle betrachten wir die Zeitentwicklung um Konvergenz zu bestätigen. Die chromoelektrischen und chromomagnetischen Feldkomponenten werden auf der Separationsachse und auf Achsen orthogonal zur Separationsachse in der Mitte zwischen Quark und Antiquark berechnet. Zusätzlich erhielten wir Ergebnisse für die Farbfelder des hybriden statischen Potentials auf einer Ebene aufgespannt durch die Separationsachse und eine dazu orthogonale Achse. Diese können ein vollständiges Bild der gluonischen Verteilung zwischen den Farbladungen liefern.

Content

1 Introduction **1**

2 SU(2) Yang-Mills-theory on the lattice **2**
2.1 Computation of the static $Q\bar{Q}$ potential in SU(2) Yang Mills theory . . . 3
2.2 Computation of the square of the chromoelectric and chromomagnetic field in SU(2) Yang-Mills-theory 4

3 Hybrid static potentials **8**

4 Results **10**
4.1 Lattice setup 10
4.2 Ordinary and hybrid static $Q\bar{Q}$ potential 10
4.3 Gluon field strength of static $Q\bar{Q}$ potential 11
4.4 Gluon field strength of hybrid static $Q\bar{Q}$ potential Π_u 14
4.5 Comparison with existing results 17

5 Conclusion **20**
5.1 Summary 20
5.2 Outlook 20

Bibliography **21**

1 Introduction

The fundamental constituents of matter, quarks, interact strongly with each other exchanging the gauge boson of Quantum chromodynamics, the gluon. QCD can be described with the SU(3)-colour gauge group. In contrast to quantum electrodynamics, which corresponds to the abelian gauge group U(1), SU(3) is non-abelian. This implies the gauge bosons to carry colour charge and consequently interact accordingly. Moreover the coupling constant of the strong force is of high magnitude for large distances and low energies. As a consequence perturbative approaches cannot be used in this regime making it very hard to describe QCD analytically. Therefore numerical solution procedures are used in form of lattice gauge theory, doing statistical simulations on a discretized space-time-lattice.

Another implication of the high coupling constant is that quarks only appear in bound states. The most simple one is the meson, consisting of a quark and an antiquark. As a quantum dynamical system mesons can be characterized by quantum numbers arising from the structure of the quark-antiquark-pair. In experiments exotic meson states were measured not explainable by this classic model. One way to explain them is by excitation of the gluonic field. Quark-antiquark states in which excited gluons contribute to the quantum numbers are called hybrid mesons.

In the past especially the static potential of the hybrid meson state was computed ([1]-[4]). This was done by modifying the spatial part of the Wilson loop to create states according to the hybrid quantum numbers covered in chapter 3. To get a better understanding of the structure of those excited gluons in a meson state one can investigate the chromoelectric and chromomagnetic field components. This is done in this thesis for an explicit example of insertions which create a trial state of a hybrid meson.

The flux tubes of an ordinary quark-antiquark pair are a well understood system that has been computed on the lattice from 1990 onwards ([5]-[7]). At the beginning of the research for this thesis the only publication about hybrid static potential flux tubes was [8] where the gluon was treated as an adjoint source. This is a very different approach than the one used in this work since the gluons are free after we indicate an excited shape.
Recently results on various hybrid static potentials were published using the very same approach as in this thesis ([9]). Those results are compared to ours in chapter 4.5.

2 SU(2) Yang-Mills-theory on the lattice

Quantum chromodynamics can be described via the colour gauge group SU(3). With the gauge group SU(2), there are only two different colour charges instead of three. This still works effectively for investigating a meson system with two static quarks, giving similar results. In addition to that the computation time is lower for SU(2) making it a good choice to obtain first qualitative results.

In SU(2) gauge theory one demands the action to be gauge invariant under SU(2) transformations. To ensure the gauge invariance of the dynamical part of the action one needs to introduce the covariant derivative. It can be expressed using link variables

$$U(x,y) = \exp\left[ig\int_x^y \mathrm{d}z_\mu \mathcal{A}_\mu(z)\right] \in SU(2) \tag{2.1}$$

where g is the coupling constant and $A_\mu = A_\mu^i \frac{\sigma_i}{2}$ the gauge field with the Pauli-matrices σ^i.

On the lattice this link variable between one site and the next at position $r = (t, x, y, z)$ in direction μ will be referred to as $U_\mu(r)$. It is used to construct gauge invariant quantities on the lattice. For notation purposes we introduce the straight path of link variables starting at r_0 and ending at $r_0 + R$ in direction μ as

$$S_\mu(r_0, R) = \prod_{k=0}^{R-1} U_\mu(r_0 + ak\hat{e}_\mu) \tag{2.2}$$

where a is the distance between two lattice sites.
The Wilson loop as a closed path of four straight paths in direction μ and ν at lattice site r with extensions R and T is defined as

$$W_{\mu\nu}(r,R,T) = Tr\left[S_\mu(r,R) * S_\nu(r+\hat{e}_\mu R, T) * S_\mu^\dagger(r+\hat{e}_\nu T, R) * S_\nu^\dagger(r,T)\right] \tag{2.3}$$

The simplest non-unit Wilson loop possible is obtained by setting $R = T = 1$ and called plaquette:

$$P_{\mu\nu}(r) = Tr\left[U_\mu(r) * U_\nu(r+a\mu) * U_\mu^\dagger(r+a\nu) * U_\nu^\dagger(r)\right] \tag{2.4}$$

2.1 Computation of the static $Q\bar{Q}$ potential in SU(2) Yang Mills theory

The correlation function for a trial state of a quark at $\mathbf{y}$ and an antiquark at $\mathbf{x}$ at $t = 0$ is given by:

$$\begin{aligned}\mathcal{C}_{Q\bar{Q}}(\mathbf{x}, t; \mathbf{y}, t) &= \langle\Omega|\mathcal{O}(\mathbf{x}, t; \mathbf{y}, t)\mathcal{O}(\mathbf{x}, 0; \mathbf{y}, 0)|\Omega\rangle \\ &= \langle\Omega|\bar{\psi}^{(Q)}(\mathbf{x}, t)U(\mathbf{x}, t; \mathbf{y}, t)\psi^{(Q)}(\mathbf{y}, t)\bar{\psi}^{(Q)}(\mathbf{x}, 0)U(\mathbf{x}, 0; \mathbf{y}, 0)\psi^{(Q)}(\mathbf{y}, 0)|\Omega\rangle\end{aligned} \tag{2.5}$$

Actually there are also colour indices appearing at the quark fields. We omit them in this work since they do not change the calculation for better readability. Via path integral formalism this correlation function can be rewritten as a function of the Wilson loop in temporal and separation direction z as shown in figure 2.1. This lengthy calculation can be found in [10] and was not done in this work. The result gives

$$C_{Q\bar{Q}}(\mathbf{x}, 0; \mathbf{y}, t) = P_+P_-e^{-2M_Q t}\langle W_{0z}(\mathbf{r}, t, R, T)\rangle \tag{2.6}$$

with

$$P_\pm = \frac{1}{2}\left(1 \pm \gamma^0\right) \tag{2.7}$$

On the other hand one can express the correlation function through time evolution of the operators and inserting a complete basis of energy eigenvalues as:

$$\begin{aligned}\mathcal{C}(t) = \langle\Omega|\mathcal{O}(t)\mathcal{O}(0)|\Omega\rangle &= \langle\Omega|e^{Ht}\mathcal{O}(0)e^{-Ht}\mathcal{O}(0)|\Omega\rangle \\ &= \sum_n \langle\Omega|e^{Ht}\mathcal{O}(0)|n\rangle\langle n|e^{-Ht}\mathcal{O}(0)|\Omega\rangle \\ &= \sum_n |\langle\Omega|\mathcal{O}(0)|n\rangle|^2 e^{-(E_n - E_\Omega)t}\end{aligned} \tag{2.8}$$

where E_n is an energy eigenvalue of the system and E_Ω the energy of vacuum. One can already see, that after giving the system enough time only the ground energy state E_0 will remain as all others are exponentially suppressed. This leads to

$$\lim_{t\to\infty}\mathcal{C}(t) = F(t)e^{-(E_0 - E_\Omega)t} = F(t)e^{-V_{Q\bar{Q}}t} \tag{2.9}$$

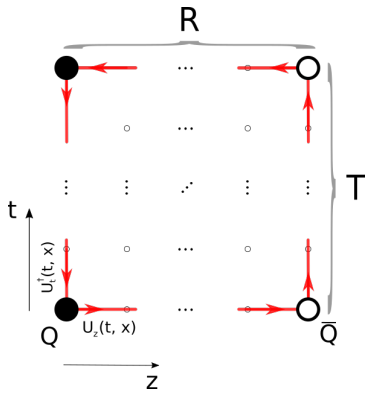

Figure 2.1: Wilson loop for computing the static quark-antiquark potential

where $V_{Q\bar{Q}}$ is the static $Q\bar{Q}$ potential and

$$F(t) = |\langle\Omega|\mathcal{O}(0)|0\rangle|^2 \tag{2.10}$$

denotes the overlap of the initial trial state with the ground state of the system. Combining 2.6 and 2.9 we obtain an expression for the static quark-antiquark potential

$$V_{Q\bar{Q}} = \lim_{a\to 0}\lim_{t\to\infty} V_{eff}(r) = \lim_{a\to 0}\lim_{t\to\infty} \frac{1}{a}\ln\left(\frac{\langle W(R,T)\rangle}{\langle W(R,T+1)\rangle}\right) \tag{2.11}$$

2.2 Computation of the square of the chromoelectric and chromomagnetic field in SU(2) Yang-Mills-theory

Due to the additional (colour) index of the E- and B-field in non-abelian gauge theories they do not represent gauge invariant quantities. To still gain information about them we take a look at the field strength tensor $F_{\mu\nu} = \partial_\mu \mathcal{A}_\nu - \partial_\nu \mathcal{A}_\mu + ig\,[\mathcal{A}_\mu, \mathcal{A}_\nu]$. On the lattice this quantity is connected to the plaquette defined in 2.4:

$$P_{\mu\nu} = \mathrm{Tr}\left[e^{iga^2 F_{\mu\nu}}\right] \tag{2.12}$$

Since a is chosen very small one can perform a second order Taylor expansion and find

$$\begin{aligned} P_{\mu\nu} &= \mathrm{Tr}\left[1 + iga^2 F_{\mu\nu} - \frac{g^2a^4}{2}F_{\mu\nu}^2 + \mathcal{O}(a^6)\right] \\ &= \mathrm{Tr}\left[1 - \frac{g^2a^4}{2}F_{\mu\nu}^2 + \mathcal{O}(a^6)\right] \quad \text{since} \quad P_{\mu\nu} \in SU(2) \\ &\approx 2 - \frac{g^2a^4}{2}\mathrm{Tr}\left(F_{\mu\nu}^2\right) \\ \Leftrightarrow \mathrm{Tr}\left(F_{\mu\nu}^2\right) &\approx \frac{2}{g^2a^4}\left(2 - P_{\mu\nu}\right) \end{aligned} \tag{2.13}$$

This means the square of the components of the field strength tensor are a gauge invariant quantity and can be measured as such. We want to measure the chromoelectric and chromomagnetic field strength in presence of a quark antiquark pair in comparison to the vacuum. Therefore we need to calculate the expectation value of $\mathrm{Tr}\left(F_{\mu\nu}^2\right)$ for this case but also subtract the vacuum contribution:

$$\langle\mathrm{Tr}\left(F_{\mu\nu}^2\right)\rangle_{Q\bar{Q}} - \langle\mathrm{Tr}\left(F_{\mu\nu}^2\right)\rangle_{vac} \tag{2.14}$$

The first step we need to take in evaluating this expression is to discuss the time-ordering operator T arising:

$$\begin{aligned} &\langle\mathrm{Tr}\left(F_{\mu\nu}^2\right)\rangle_{Q\bar{Q}} \\ &= \frac{1}{Z}\int DAD\bar{\psi}^{(Q)}D\psi^{(Q)}T\left\{\mathcal{O}(\mathbf{x},t;\mathbf{y},t)F_{\mu\nu}(\mathbf{z},t/2)\mathcal{O}(\mathbf{x},0;\mathbf{y},0)\right\}e^{-(S_Q[\bar{\psi}^{(Q)},\psi^{(Q)},A]+S_G[A])} \end{aligned} \tag{2.15}$$

For the chromomagnetic part we know that $\mu, \nu \in \{1, 2, 3\}$. There are no temporal components in this part of the field strength tensor. So time-ordering is fulfilled without changes.

For the chromoelectric part of the field strength we can consider $\nu \in 1, 2, 3$ and $\mu = 0$ without loss of generality. To simplify calculations we assume temporal gauge $A_0 = 0$. For the euclidean field strength tensor this leads to

$$F_{0j} = -i\partial_0 A_j \tag{2.16}$$

Since we operate on the lattice the derivative can be rewritten as

$$\begin{aligned} F_{0j}^2\left(l + \frac{1}{2}a\hat{e}_0\right) &= \left[-i\frac{A_j(l + a\hat{e}_0) - A_j(l)}{a}\right]^2 \\ &= \frac{1}{a^2}\left[-A_j(l + a\hat{e}_0)^2 - A_j(l)^2 + A_j(l + a\hat{e}_0)A_j(l) + A_j(l)A_j(l + a\hat{e}_0)\right] \end{aligned} \tag{2.17}$$

where l is a lattice coordinate in space time. Performing time-ordering this expression yields

$$TF_{0j}^2\left(l + \frac{1}{2}a\hat{e}_0\right) = \frac{1}{a^2}\left[-A_j(l + a\hat{e}_0)^2 - A_j(l)^2 + 2A_j(l + a\hat{e}_0)A_j(l)\right] \tag{2.18}$$

We can also explicitly write the plaquette in temporal gauge and Taylor expand the exponential functions to obtain

$$\begin{aligned} P_{0j}(l) &= \mathrm{Tr}\left[e^{igaA_j(l+a\hat{e}_0)}e^{igaA_j(l)}\right] \\ &= \mathrm{Tr}\left[1 + \frac{g^2a^2}{2}\left[-A_j(l + a\hat{e}_0)^2 - A_j(l)^2 + A_j(l + a\hat{e}_0)A_j(l) + A_j(l)A_j(l + a\hat{e}_0)\right]\right] \end{aligned} \tag{2.19}$$

where in the last step was used that the imaginary part of the trace of SU(2) matrices is always zero. As we can see the right side of 2.18 reappears in 2.19. Plugging this in we obtain an time-ordered expression of the square of the chromoelectric field:

$$TF_{0j}^2\left(l + \frac{1}{2}a\hat{e}_0\right) = \frac{2}{g^2a^4}\left(P_{0j} - 2\right) \tag{2.20}$$

Now we can use the obtained expression for the square of the chromoelectric field 2.20 and chromomagnetic field 2.13 and plug those into 2.14:

$$\langle \mathrm{Tr}\left(F_{0j}^2\right)\rangle_{Q\bar{Q}} - \langle \mathrm{Tr}\left(F_{0j}^2\right)\rangle_{vac} = \frac{2}{g^2a^4}\left[\langle P_{0j}\rangle_{Q\bar{Q}} - \langle P_{0j}\rangle_{vac}\right] \tag{2.21}$$

$$\langle \mathrm{Tr}\left(F_{kl}^2\right)\rangle_{Q\bar{Q}} - \langle \mathrm{Tr}\left(F_{kl}^2\right)\rangle_{vac} = \frac{2}{g^2a^4}\left[\langle P_{kl}\rangle_{vac} - \langle P_{kl}\rangle_{Q\bar{Q}}\right] \tag{2.22}$$

The expectation value of the plaquette in vacuum can immediately be numerically computed. Still $\langle P_{\mu\nu}\rangle_{Q\bar{Q}}$ needs to be determined. In order to do this we first consider the plaquette temporarily exactly between the quark-antiquark-pairs in spacetime in path integral formalism:

$$\begin{aligned} &\langle\Omega|\mathcal{O}(\mathbf{x}, t; \mathbf{y}, t)P_{\mu\nu}(\mathbf{z}, t/2)\mathcal{O}(\mathbf{x}, 0; \mathbf{y}, 0)|\Omega\rangle \\ &= \frac{1}{Z}\int DAD\bar{\psi}^{(Q)}D\psi^{(Q)}\mathcal{O}(\mathbf{x}, t; \mathbf{y}, t)P_{\mu\nu}(\mathbf{z}, t/2)\mathcal{O}(\mathbf{x}, 0; \mathbf{y}, 0)e^{-(S_Q[\bar{\psi}^{(Q)},\psi^{(Q)},A]+S_G[A])} \\ &= P_+P_-e^{2M_Qt}\left\langle W_{0z}(\mathbf{r}, 0, R, T)\cdot P_{\mu\nu}(\mathbf{z}, T/2)\right\rangle \end{aligned} \tag{2.23}$$

The steps of solving this path integral with the plaquette the same as without (see 2.6).

On the other hand we consider the energy eigenvalue representation of $\langle P_{\mu\nu}\rangle_{Q\bar{Q}}(\mathbf{z}, t/2)$ to get a connection to $\langle P_{\mu\nu}\rangle_{Q\bar{Q}}(\mathbf{z}, 0)$:

$$\begin{aligned}
&\langle\Omega|\mathcal{O}(\mathbf{x},t;\mathbf{y},t)P_{\mu\nu}(\mathbf{z},t/2)\mathcal{O}(\mathbf{x},0;\mathbf{y},0)|\Omega\rangle \\
&= \langle\Omega|e^{Ht}\mathcal{O}(\mathbf{x},0;\mathbf{y},0)e^{-Ht}e^{\frac{1}{2}Ht}P_{\mu\nu}(\mathbf{z},0)e^{-\frac{1}{2}Ht}\mathcal{O}(\mathbf{x},0;\mathbf{y},0)|\Omega\rangle \\
&= \sum_{n,m}\langle\Omega|e^{Ht}\mathcal{O}(\mathbf{x},0;\mathbf{y},0)|n\rangle\langle n|e^{-\frac{1}{2}Ht}P_{\mu\nu}(\mathbf{z},0)e^{-\frac{1}{2}Ht}|m\rangle\langle m|\mathcal{O}(\mathbf{x},0;\mathbf{y},0)|\Omega\rangle \\
&= \sum_{n,m}\langle\Omega|\mathcal{O}(\mathbf{x},0;\mathbf{y},0)|n\rangle\langle n|P_{\mu\nu}(\mathbf{z},0)|m\rangle\langle m|\mathcal{O}(\mathbf{x},0;\mathbf{y},0)|\Omega\rangle\, e^{-\left(\frac{1}{2}E_n+\frac{1}{2}E_m-E_\Omega\right)t} \qquad (2.24)
\end{aligned}$$

For $t\to\infty$ all eigenstates except for the ground state vanish because they are exponentially suppressed. This leads to a very similar result to the two-point-correlation function for a static-quark-antiquark pair in 2.9:

$$\begin{aligned}
&\lim_{t\to\infty}\langle\Omega|\mathcal{O}(\mathbf{x},t;\mathbf{y},t)P_{\mu\nu}(\mathbf{z},t/2)\mathcal{O}(\mathbf{x},0;\mathbf{y},0)|\Omega\rangle \\
&= \langle\Omega|\mathcal{O}(\mathbf{x},0;\mathbf{y},0)|0\rangle\langle 0|P_{\mu\nu}(\mathbf{z},0)|0\rangle\langle 0|\mathcal{O}(\mathbf{x},0;\mathbf{y},0)|\Omega\rangle\, e^{-(E_0-E_\Omega)t} \\
&= C_{Q\bar{Q}}(\mathbf{x},0;\mathbf{y},t)\cdot\langle 0|P_{\mu\nu}(\mathbf{z},0)|0\rangle \qquad (2.25)
\end{aligned}$$

Comparing 2.23, 2.24 and 2.6 we obtain

$$\langle P_{\mu\nu}\rangle_{Q\bar{Q}}(\mathbf{z},0) = \frac{\langle W_{0z}(\mathbf{r},0,R,T)\cdot P_{\mu\nu}(\mathbf{z},T/2)\rangle}{\langle W_{0z}(\mathbf{r},0,R,T)\rangle} \qquad (2.26)$$

Returning to 2.21 and 2.22 we get the final expression for the square of chromoelectric and chromomagnetic field on the lattice

$$\langle E_j(\mathbf{z})^2\rangle_{Q\bar{Q}} - \langle E_j^2\rangle_{vac} = \frac{2}{g^2a^4}\left[\frac{\langle W\cdot P_{0j}(T/2,\mathbf{z})\rangle}{\langle W\rangle} - \langle P_{0j}\rangle\right] \qquad (2.27)$$

$$\langle B_j(\mathbf{z})^2\rangle_{Q\bar{Q}} - \langle B_j^2\rangle_{vac} = \frac{2}{g^2a^4}\left[\langle P_{kl}\rangle - \frac{\langle W\cdot P_{kl}(T/2,\mathbf{z})\rangle}{\langle W\rangle}\right] \qquad (2.28)$$

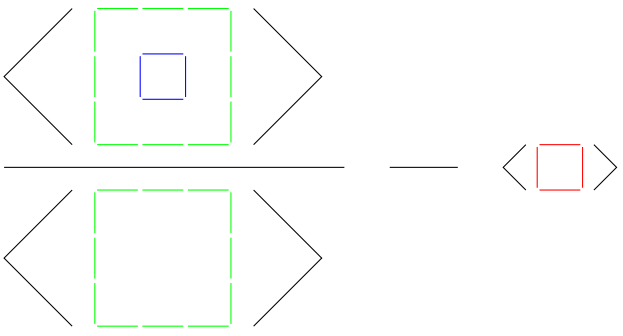

Figure 2.2: Graphical representation of the lattice formula to compute the square of the chromoelectric field.
green: The Wilson loop spatially and temporarily connecting the quark and antiquark pair
blue: The Plaquette positioned temporarily in the middle of both states and at the spatial coordinate where the field is evaluated
red: A plaquette

The calculation of E- and B-Field via 2.28 consists of three parts as sketched in figure 4.1. The two-point-correlation functions of Wilson loop and Plaquette can be computed according to 2.3 and 2.4.

To compute the three-point-correlation-function of $\langle W \cdot P_{\mu\nu}(T/2, \mathbf{z})\rangle$ one has to determine the values of plaquettes in all directions. Taking a closer look at the plaquette $P_{\mu\nu}(r)$ as defined in 2.4 this leads to a problem. While for the limit $a \to 0$ one can consider the plaquette to be evaluated at r, for a finite a the plaquette yields a field at $\tilde{r} = r + \frac{1}{2}a\hat{e}_\mu + \frac{1}{2}a\hat{e}_\nu$ with $\hat{e}_\mu$ being the four-unit-vector in μ direction.
This makes results hard to compare. One cannot measure all field components at a certain lattice site because they are always shifted by $\frac{1}{2}$ in their respective directions.
To solve this problem we average the plaquettes around a lattice site in the directions μ and ν:

$$P'_{\mu\nu}(r) = \frac{1}{4}\left[P_{\mu\nu}(r) + P_{\mu\nu}(r - a\hat{e}_\mu) + P_{\mu\nu}(r - a\hat{e}_\nu) + P_{\mu\nu}(r - a\hat{e}_\mu - a\hat{e}_\nu)\right] \tag{2.29}$$

We immediately notice that $\lim_{a\to 0} P'_{\mu\nu}(r) = \lim_{a\to 0} P_{\mu\nu}(r)$ making $P'_{\mu\nu}(r)$ an equivalent quantity in the continuum limit. It turns out to be a lot better for comparing the field strength component though since they are computed at r instead of $\tilde{r}$.

The separations on the lattice need to be chosen in a way that the plaquette is located exactly between the two spatial parts of the Wilson loop in temporal direction at $T/2$. So we are restricted to even T. We do not consider $T = 0$ because the system would not get an opportunity to find a physical state according to its Hamiltonian. This leads to $T = 2a$ being the smallest possible temporal extension of the Wilson loop. Now one needs to observe the behaviour of field strength as a function of time to find the approximate threshold when the ground state is reached.

The results obtained for the square of chromoelectric and chromomagnetic field strength are in lattice units and do not represent the actual values. To obtain those a renormalization procedure needs to be performed which is a complicated and lengthy task itself. Thus it is not done in this work.

3 Hybrid static potentials

Hybrid mesons arise when excited gluons contribute to the quantum numbers of the particle. This affects the potential between quark and antiquark. The static potential of ordinary quark-antiquark is computed via 2.11 with the Wilson loop 2.3 in temporal and one spatial direction. To compute the hybrid static potential the part of the Wilson loop in spatial direction is modified according to arising quantum numbers. This results in spatial Wilson lines off the separation axis, referred to as 'insertions'.

There are 3 hybrid static potential quantum numbers noted as $|L|^{P_x}_{\mathcal{P}\circ\mathcal{C}}$ sketched in figure 3.1:

1. $|L| \in \{\Sigma \doteq 0, \Pi \doteq 1, \Delta \doteq 2\}$ characterizes the angular momentum of the state with respect to the separation axis of the quark-antiquark pair.
   This quantum number is realized by rotating the insertion around the separation axis and weighting them according to 2-dimensional spherical harmonics. For an insertion I this leads to the sum

$$S_L = \sum_{k=0}^{3} e^{iLk\frac{\pi}{2}} \hat{R}\left(\frac{k\pi}{2}\right) I \tag{3.1}$$

   where $\hat{R}(\phi)$ is a rotation operator around the separation axis.

2. $\mathcal{P}\circ\mathcal{C} \in \{g \doteq +, u \doteq -\}$ corresponds to a combination of parity and charge conjugation
   In practice this quantum number is the behaviour under spatial reflection of all insertions along the point in the middle between quark and antiquark and then reversal of the direction of the paths.

3. $P_x \in \{+, -\}$ describes the inversion along an axis perpendicular to the separation axis of quark and antiquark

In this work an explicit insertion which yields the trial state for Π_u is used. It corresponds to angular momentum $|L| = 1$ and parity and charge conjugation "$-$". We do not take the last quantum number P_x into account since hybrid states with angular momentum

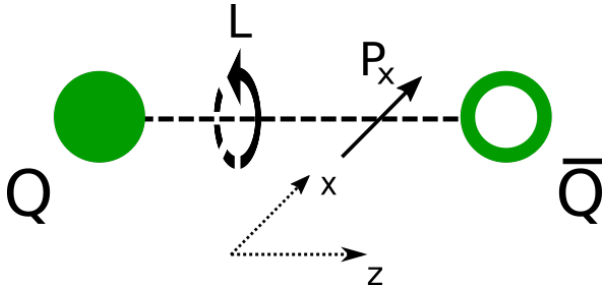

Figure 3.1: Schematic representation of quantum numbers of hybrid static potentials

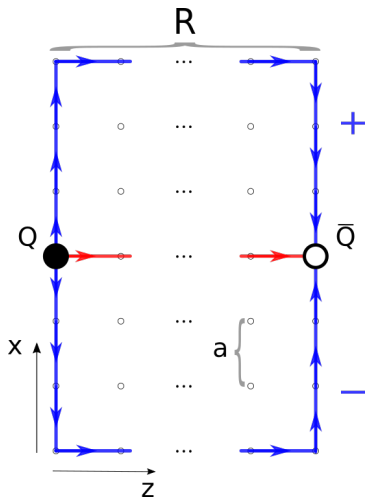

Figure 3.2: Spatial insertion of the Wilson loop for hybrid static potential Π_u.

The separation axis is indicated by the dashed line but does not contribute to the modified Wilson Loop. The insertions in direction of x and -x move three links away from the separation axis and proceed parallel. One of them contributes with a positive sign and the other with a negative one.

$|L|= 1$ are degenerate in this quantum number. The insertions we use to generate this hybrid static potential is one of the most simple ones shown and explained in figure 3.2. The modified Wilson loop is computed as

$$\begin{aligned} W_{\Pi_u}(r,R,T) = &[S_+(r,R) - S_-(r,R)] \cdot S_t(r+\hat{e}_z R,T) \\ &\cdot \left[S_+^\dagger(r+\hat{e}_z T,R) - S_-^\dagger(r+\hat{e}_z T,R)\right] \cdot S_t^\dagger(r,T) \end{aligned} \tag{3.2}$$

where $S_+(r,R)$ denotes the upper insertion path in figure 3.2 and S_- the lower one with quark position r and separation distance of the quark-antiquark pair R.
We immediately notice that this trial state is not symmetric in all directions perpendicular to the separation axis. There is a distinguished axis along the insertions. This will be referred to as x-direction. Consequently the last axis perpendicular to the insertions will be the y-axis.

4 Results

4.1 Lattice setup

For the Wilson loop APE smearing is used. The plaquette is computed without smearing since a smeared plaquette would result in a different formula than 2.28. All the following lattice calculations were done on a $18^3 \cdot 18$ SU(2) lattice. The configurations were generated by a Monte-Carlo heatbath algorithm ([12]). Only every hundredth configuration was taken to minimize correlations between the results. The APE smearing parameters are $N_{APE} = 20$ and $\alpha = 0.5$. Errors were calculated with the Jacknife method [11].

To obtain as many statistics as possible from each configuration the observable is relocated and rotated in spatial directions on the lattice. With this one obtains $18^4 * 3 = 314928$ results from each configuration to average over.

To compute the static potential discussed in 4.2 $\beta = 2.3$ was used which corresponds to $a \approx 0.14fm$. The results were obtained averaging over 700 configurations.

To compute the square of the chromoelectric and chromomagnetic fields $\beta = 2.5$ corresponding to $a \approx 0.073fm$ was used averaging over 2000 configurations.

4.2 Ordinary and hybrid static $Q\bar{Q}$ potential

To compute the potential of a static $Q\bar{Q}$ state the Wilson loop needs to be evaluated according to 2.11. In figure 4.1 the effective potential is calculated for all $T \leq 8$ and $R \leq 8$. We can observe the convergence of the effective potential to the actual potential in this plot. On the other hand errors become larger the higher T and R. One needs to come to a compromise between low errors and convergence.

Taking an explicit look at the ordinary static $Q\bar{Q}$ effective potential, shorter separations between quark and antiquark lead to a faster convergence of the effective potential. Also the errors remain very small for $R \leq 5$ even for large temporal separations. For $R \geq 6$ the errors become significant for $T \geq 5$. Still the data is sufficiently precise up to $T = 3$ across all separations to yield meaningful results. Additionally values of the effective potential are constant within their errors between $R = 2$ and $R = 3$ indicating that the plateau of convergence is already reached. Therefore we can fit a constant to those values obtaining the potential in lattice units shown in the right pictures.

The effective potential of the hybrid static state shows large to very large errors for $T \geq 4$. Again between $T = 2$ and $T = 3$ a convergence within the errors is reached while the error bars are acceptable especially for smaller R.

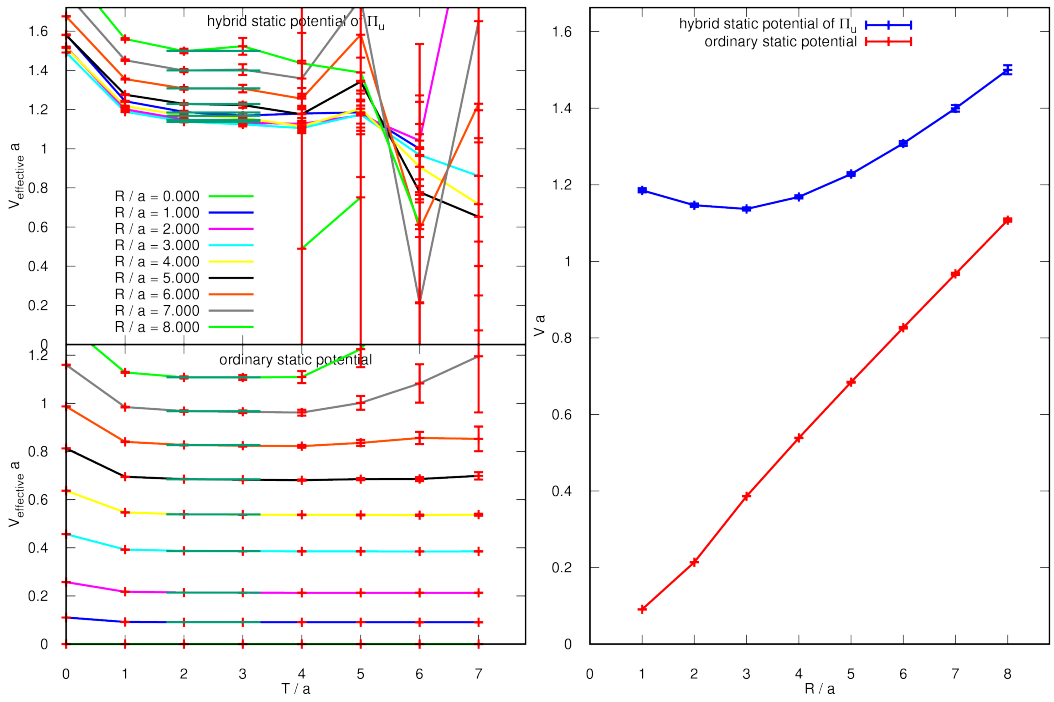

Figure 4.1: left: effective potentials of ordinary static $Q\bar{Q}$ and hybrid static $Q\bar{Q}$ Π_u for different temporal and spatial separations
right: the resulting potentials for those states

The hybrid static potential is higher than the ordinary static potential for all separations R. A different shape of the plot for low R is noticeable. The ordinary static potential starts out linearly increasing but the hybrid one actually starts decreasing up to the minimum at $R = 3$. Taking a look at large distances both behave similarly: The potential increases linearly as a function of the distance. The graph for the ordinary case rises faster though.

4.3 Gluon field strength of static $Q\bar{Q}$ potential

In all our numerical computations of the square of chromoelectric and chromomagnetic field the separation of quark-antiquark pair is $R = 6a$. In figure 4.2 we take a look at the time evolution of the field strength components on the separation axis. While analysing the behaviour of an observable as a function of time one has to pay close attention to the errors. The values for $T \geq 6a$ are impossible to compare due to their large errors. However they do need to support the result for lower T within their error bars. The differences between values for $T = 2a$ and $T = 4a$ are very small. Especially in the middle between quark and antiquark the ground state seems to be reached already at $T = 2a$.

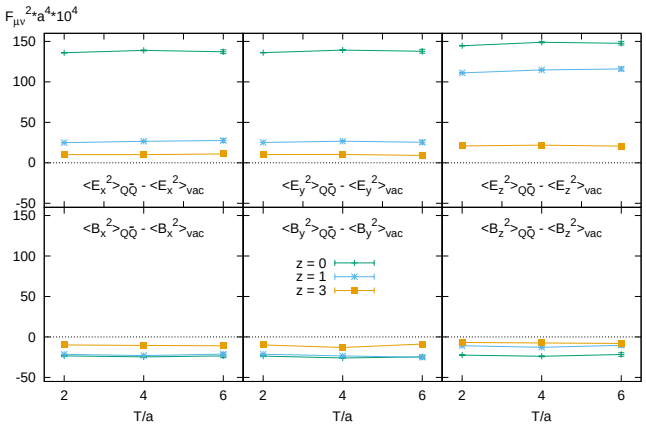

Figure 4.2: The field strength in components for different locations on the separation axis z as a function of T. Quark and antiquark are located at $z = 0$ and $z = 6a$ respectively.
$F^2_{\mu\nu,err}(T = 2a) \approx 2 * 10^{-5}$
$F^2_{\mu\nu,err}(T = 4a) \approx 3 * F^2_{\mu\nu,err}(T = 2a)$
$F^2_{\mu\nu,err}(T = 6a) \approx 10 * F^2_{\mu\nu,err}(T = 2a)$

The small deviations at the quark position $z = 0$ are almost negligible due to the large field strength there. All in all one can obtain reasonable results even for $T = 2a$. Since the errors are very small it seems best to use a higher temporal separation, $T = 4a$ being a suitable compromise. Therefore for the ordinary static quark-antiquark potential $T = 4a$ will be computed.

In figure 4.3 we take a look at the fields on the separation axis. At the positions of charges $r = 0$ and $r = 6$ the absolute values of all components is the largest. Also contributions of the chromoelectric and chromomagnetic field strength are even across all components respectively. It seems like the other charge has no influence on the chromoelectromagnetic field components at the charges position. This also holds for $r \leq 0a$ and $r \geq 6a$. Between the quarks the z-component of both E- and B-field are distinguished while the x- and y-components remain identical due to symmetry of the Wilson loop.

The contribution of the E_z-component to the energy density is by far the largest, while the B-field is more dominant orthogonal to the separation axis. In between the quarks all field components become constant forming a flux tube.

To get a better picture of the spatial extent of the flux tube in figure 4.4 the fields are evaluated on an axis orthogonal to z. We do not consider this for all z but for the most interesting ones at the charges position $z = 0$ (which is identical to $z = R$) and in the middle between quark and antiquark $z = R/2$ where a flux tube structure is apparent. We choose this axis to be the x-axis. In the middle between quark and antiquark the choice of the axis does not affect the result due to rotational symmetry around the z-axis. At the charges the x component of the fields is distinguished. The behaviour of all components is very similar, their absolute value becomes smaller the larger x becomes. At $r \geq 5$ all field components are 0 within their errors.

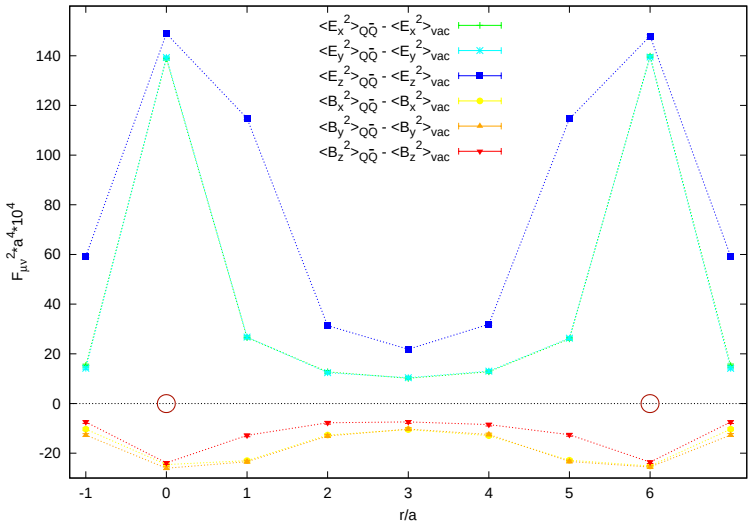

Figure 4.3: Square of chromoelectric and chromomagnetic field on the separation axis for static $Q\bar{Q}$ potential
(quark, antiquark positions at R/a = 0 and R/a = 6)

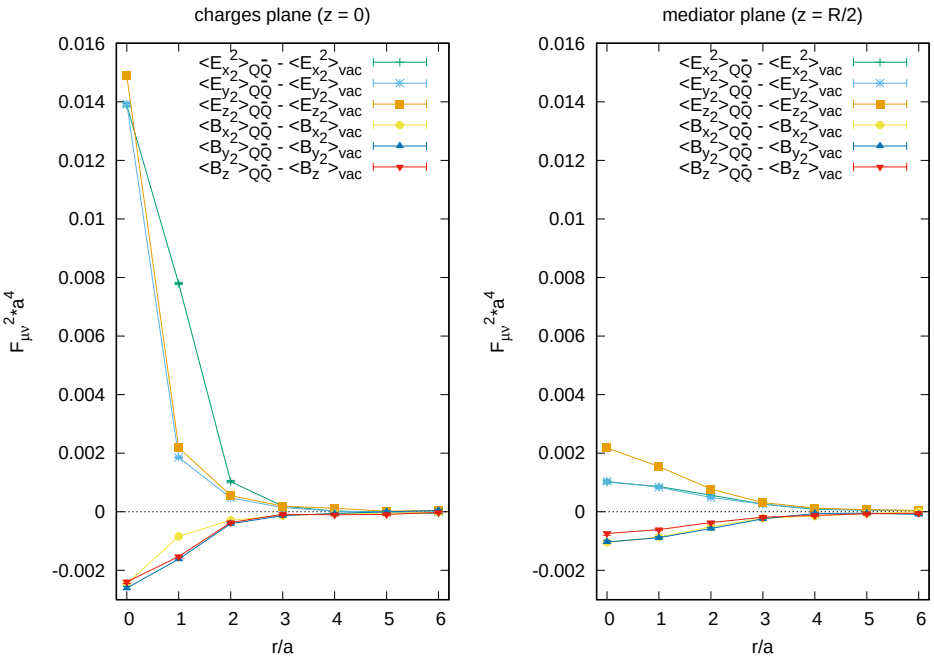

Figure 4.4: E- and B-field on charges and mediator x-axis for static $Q\bar{Q}$ potential

Our results are in agreement with results from [7].

It seems like we can interpret maxima in chromoelectric field strength and minima in chromomagnetic field strength at the same time connecting quark and antiquark as flux tubes transporting colour charge via unexcited gluons. This will be something to look out for when investigating exotic states in the next chapter.

4.4 Gluon field strength of hybrid static $Q\bar{Q}$ potential Π_u

First of all the time evolution needs to be investigated. T has to be even as before since the modifications only affect the spatial part of the Wilson loop. In figure 4.5 one can right away omit all $T \geq 6a$ due to large errors. Differences between $T = 2a$ and $T = 4a$ can be neglected for stronger field strength at $z = 0$ and $z = a$. In between the quarks at $z = 3a$ the values for $T = 2a$ are within the errors supported by the values for $T = 4a$. This needs to be treated carefully though due to the high relative error for $T = 4$ not distinguishing the signal from zero clearly. Since the errors for $T = 4$ are too high, no meaningful results can be obtained for these temporal separations without increasing the statistics significantly. Therefore we consider $T = 2$.

First of all the field components are computed on the separation axis as shown in figure 4.6. Comparing the results to figure 2.28 the field strength components look very similar at the charges positions.

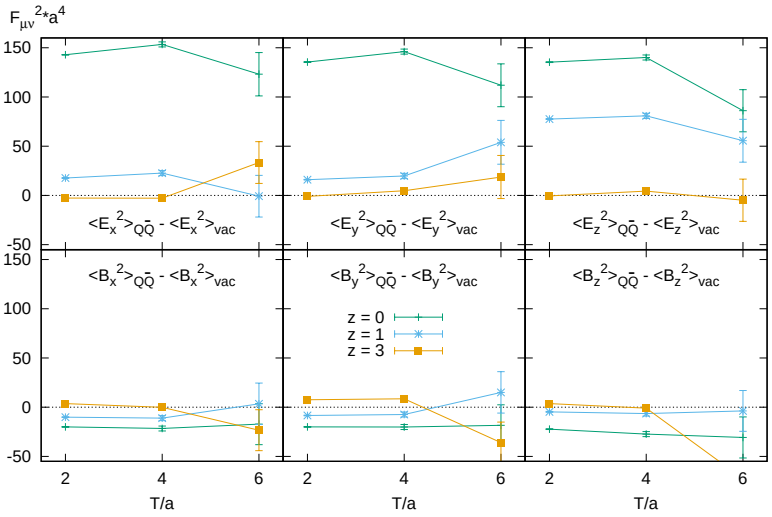

Figure 4.5: Time evolution of field strength components for hybrid static potential Π_u on the separation axis.
$F^2_{\mu\nu,err}(T = 2) \approx 4 * 10^{-5}$
$F^2_{\mu\nu,err}(T = 4) \approx 6 * F^2_{\mu\nu,err}(T = 2)$
$F^2_{\mu\nu,err}(T = 6) \approx 50 * F^2_{\mu\nu,err}(T = 2)$

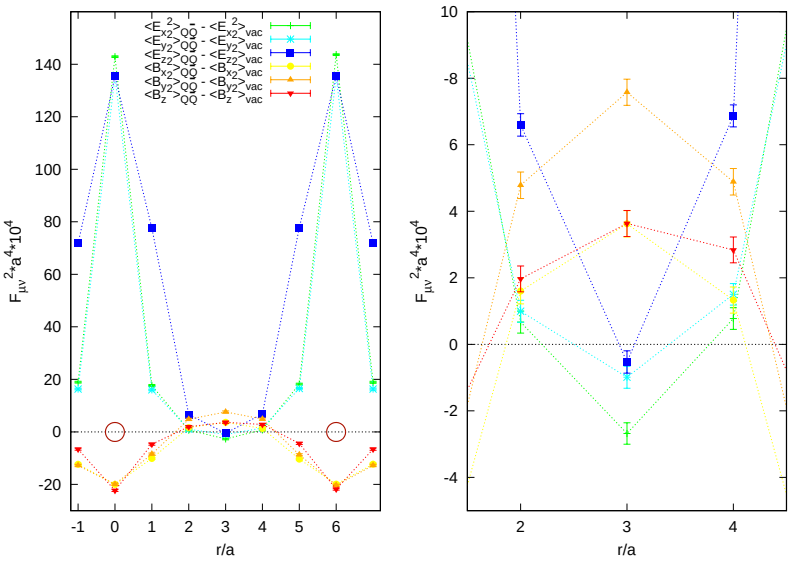

Figure 4.6: Square of chromoelectric and chromomagnetic field on the separation axis of static $Q\bar{Q}$ potential for hybrid state Π_u
(quark, antiquark positions at R/a = 0 and R/a = 6)

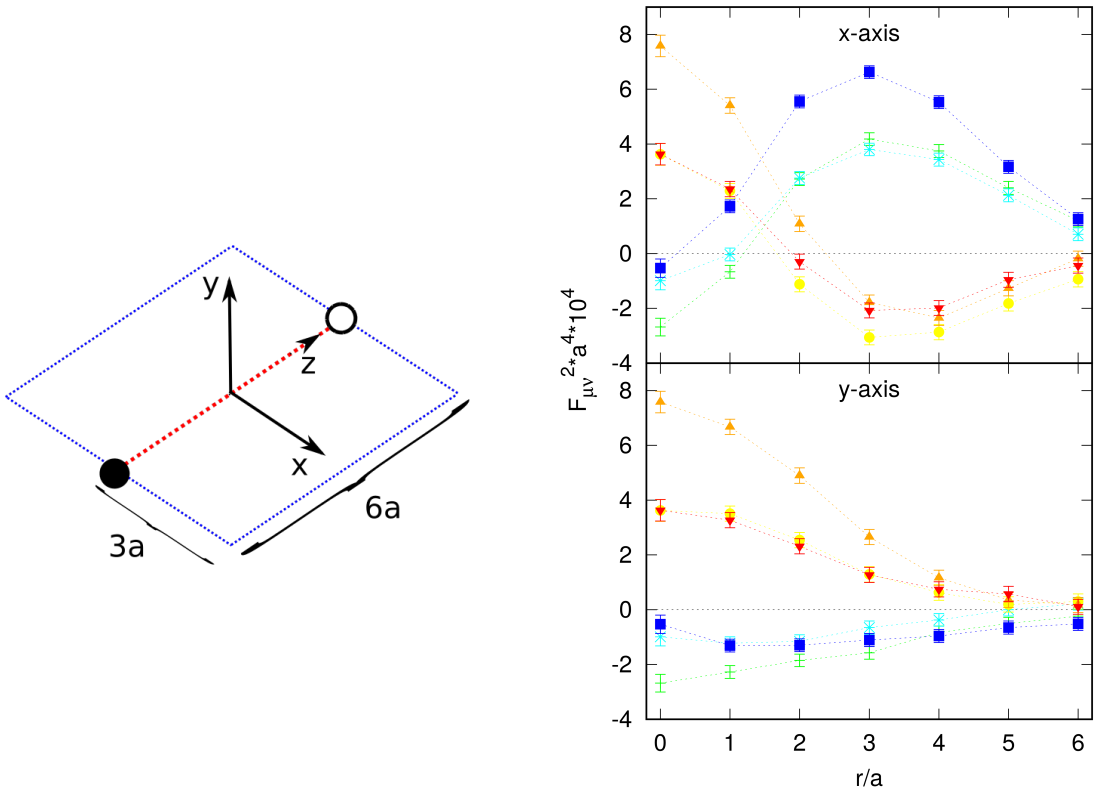

Figure 4.7: Square of chromoelectric and chromomagnetic field on axes orthogonal to the separation axis in the middle between quark and antiquark for hybrid static potential of Π_u.
The results are symmetric with respect to spatial inversion perpendicular to the separation axis and therefore merged in order to get better statistics.

Exactly in the middle between quark and antiquark all the chromoelectric field strength components seem to vanish or even become slightly negative. On the other hand the chromomagnetic field strength components are clearly positive, the B_y - component being the most dominant. Taking a look at W_{Π_u} and figure 3.2 again this seems reasonable since the plaquette that computes the B_y-component lies in the plane of insertions.

The most interesting differences seem to be exactly halfway between quark and antiquark. To get a better picture of the fields strength behaviour at this position we consider the field components on axes perpendicular to the separation axis in the middle between quark and antiquark (figure 4.7). Unlike the ordinary static $Q\bar{Q}$ this state is not invariant under rotations around the z-axis. We take a closer look at the axes in x and y-direction.
In x-direction along the insertion axis chromoelectric field strength rises up until $r = 3a$ where we observe a maximum and domination of the E_z component. At the same time chromomagnetic field strength decreases having a minimum at $r = 3a$. This looks very similar to the field for ordinary static potentials on the separation axis, indicating chromoelectric field lines in z-direction at this position. For higher r the fields converge to zero.
In y-direction there is a small decrease of field strength in the E_y and E_z component from $r = 0$ to $r = a$. For $r \geq 2a$ all components are monotonically decreasing in their absolute value.

Clearly the xz-plane, being the plane of insertions, turns out to be the most interesting one. Therefore in figure 4.8 we take a look at the field on the xz-plane visualized via heatmap. This shows very well the large chromomagnetic field in the middle between quark and antiquark suppressing the chromoelectric field.

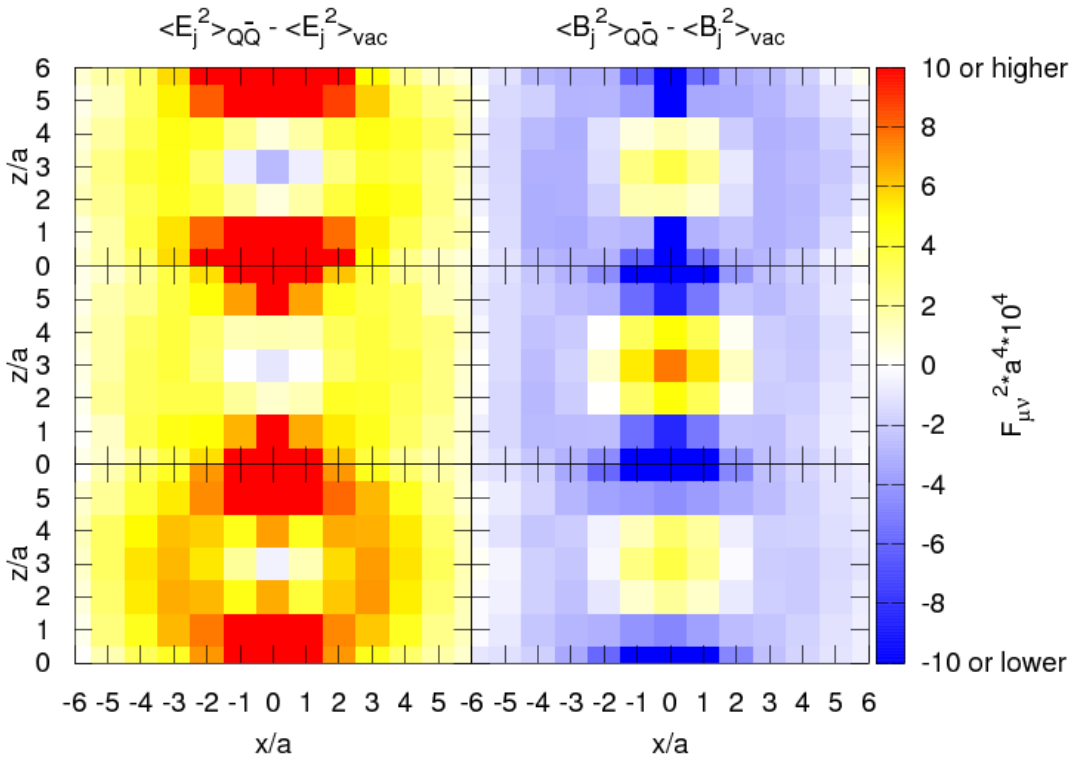

Figure 4.8: Heatmap of all field strength components for Π_u
Quark and antiquark are positioned at $x = z = 0$ and $z = 6$, $x = 0$ respectively

This also results in the chromoelectric parts maxima which can be interpreted as the interaction between quark and antiquark not being able to happen in a straight line but instead in a circular form around the excitation.

At this point it is important to take the separation of quark and antiquark into account, which was chosen to be $R = 6$. As we can observe very well in the left part of figure 4.7 the insertions have a square-like form for this separation. For different separations we would expect the circular form of the chromoelectric field in figure 4.8 to become more ellipse-like accordingly.

4.5 Comparison with existing results

Recently the gluon fields for hybrid static flux tubes were computed in [9]. Apart from the different insertions that were used, the most obvious difference is the rotational symmetry around the separation axis of the results in [9]. To understand this we need to take a closer look at the quantum number of angular momentum on the lattice. Considering 3.1 for the explicit case of $L = \pm 1$ leads to

$$\begin{aligned} S_{+1} &= \left[1 + i\hat{R}\left(\frac{\pi}{2}\right) - \hat{R}\left(\pi\right) - i\hat{R}\left(\frac{3\pi}{2}\right)\right] I \\ S_{-1} &= \left[1 - i\hat{R}\left(\frac{\pi}{2}\right) - \hat{R}\left(\pi\right) + i\hat{R}\left(\frac{3\pi}{2}\right)\right] I \end{aligned} \tag{4.1}$$

In this work we consider the quantum number $|L|$ though. This amounts to average over both angular momenta:

$$\begin{aligned} S_x &= \frac{1}{2}\left(S_{+1} + S_{-1}\right) = \left[1 - \hat{R}\left(\pi\right)\right] I \\ S_y &= \frac{1}{2}\left(S_{+1} - S_{-1}\right) = \left[i\hat{R}\left(\frac{\pi}{2}\right) - i\hat{R}\left(\frac{3\pi}{2}\right)\right] I \end{aligned} \tag{4.2}$$

The degree of freedom lost by taking the absolute value of angular momentum is included by the quantum number P_x. States with $|L| = 1$ are degenerate in this quantum number though.
In this work we compute S_x which yields non-rotational invariant results. In [9] on the other hand S_{+1} is used. For those states a different set of quantum numbers was used:

1. In [9]: Angular momentum L and parity and charge conjugation $P \circ C$
2. In this work: Absolute value of angular momentum $|L|$, parity and charge conjugation $P \circ C$ and behaviour under spatial inversion along the x-axis P_x

In the following we show that the results in the first set of quantum numbers can be derived from results in the second one.

Let $\mathcal{O}_x(t)$ be the operator creating a trial state similar to the one discussed in this work that lies in the x-z-plane. Also we introduce $\mathcal{O}_y(t)$ to be the same state rotated by $\pm\frac{\pi}{2}$ around the z-axis lying in the y-z-plane. Then we can write the operator used in [9] as

$$\mathcal{O}(t) = \frac{1}{\sqrt{2}}\left(\mathcal{O}_x(t) \pm i\mathcal{O}_y(t)\right) \tag{4.3}$$

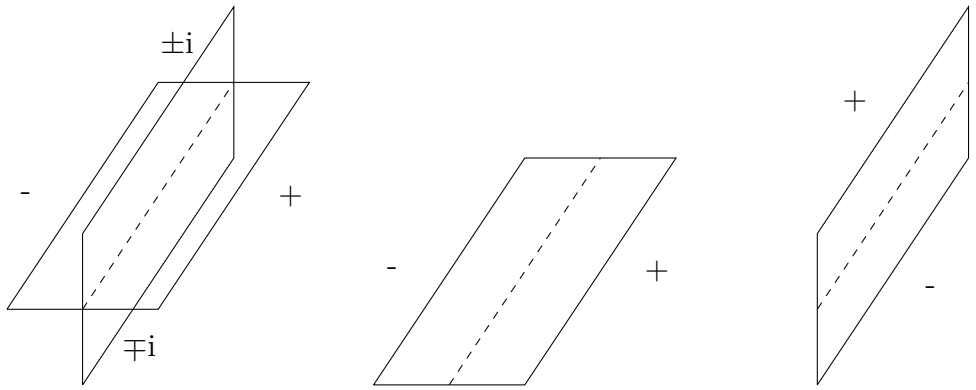

(a) $\mathcal{O}$ **(b)** $\mathcal{O}_x$ **(c)** $\mathcal{O}_y$

Figure 4.9: Sketch of $\mathcal{O}$ being decomposed in a part in xz-plane and a part in yz-plane. This works for an arbitrary insertion I.

This identity is geometrically illustrated in figure 4.9. Now we take a look at the trial state of the three point correlator created by $\mathcal{O}(t)$ and insert two sets of eigenstates of energy n, m and behaviour under spatial inversion along the x-axis $P_{x,1}, P_{x,2}$.

$$
\begin{aligned}
&\langle\Omega|\,\mathcal{O}^\dagger(t_2)F^2_{\mu\nu}(t_1)\mathcal{O}(t_0)\,|\Omega\rangle \\
&= \sum_{n,m,P_{x,1},P_{x,2}} \langle\Omega|\mathcal{O}^\dagger(t_2)|n,P_{x,1}\rangle\,\langle n,P_{x,1}|F^2_{\mu\nu}(t_1)|m,P_{x,2}\rangle\,\langle m,P_{x,2}|\mathcal{O}(t_0)|\Omega\rangle \\
&\overset{(*)}{=} \frac{1}{2}\sum_{n,m}\Big(\langle\Omega|\mathcal{O}^\dagger_x(t_2)|n,-\rangle\,\langle n,-|F^2_{\mu\nu}(t_1)|m,-\rangle\,\langle m,-|\mathcal{O}_x(t_0)|\Omega\rangle \\
&\qquad + \langle\Omega|\mathcal{O}^\dagger_y(t_2)|n,+\rangle\,\langle n,+|F^2_{\mu\nu}(t_1)|m,+\rangle\,\langle m,+|\mathcal{O}_y(t_0)|\Omega\rangle \\
&\qquad \pm i\,\langle\Omega|\mathcal{O}^\dagger_x(t_2)|n,-\rangle\,\langle n,-|F^2_{\mu\nu}(t_1)|m,+\rangle\,\langle m,+|\mathcal{O}_y(t_0)|\Omega\rangle \\
&\qquad \mp i\,\langle\Omega|\mathcal{O}^\dagger_y(t_2)|n,+\rangle\,\langle n,+|F^2_{\mu\nu}(t_1)|m,-\rangle\,\langle m,-|\mathcal{O}_x(t_0)|\Omega\rangle\Big) \\
&\overset{(**)}{=} \frac{1}{2}\sum_{n,m}\Big(\langle\Omega|\mathcal{O}^\dagger_x(t_2)|n,-\rangle\,\langle n,-|F^2_{\mu\nu}(t_1)|m,-\rangle\,\langle m,-|\mathcal{O}_x(t_0)|\Omega\rangle \\
&\qquad + \langle\Omega|\mathcal{O}^\dagger_y(t_2)|n,+\rangle\,\langle n,+|F^2_{\mu\nu}(t_1)|m,+\rangle\,\langle m,+|\mathcal{O}_y(t_0)|\Omega\rangle\Big)
\end{aligned}
\tag{4.4}
$$

using

$$
(*) \qquad \mathcal{O}_x(t) \xrightarrow{P_x} -\mathcal{O}_x(t) \qquad \mathcal{O}_y(t) \xrightarrow{P_x} \mathcal{O}_y(t) \tag{4.5}
$$

$$
(**) \qquad E^2 \xrightarrow{P_x} E^2 \qquad B^2 \xrightarrow{P_x} B^2 \tag{4.6}
$$

The first part of this result in 4.4 is exactly what is computed in this work. The second one can be obtained by rotating the first one by an angle of $\pm\frac{\pi}{2}$ also leading to the same result rotated by this angle. In practice this means that adding up results along the x-axis with ones along the y-axis provides those only depending on distance from the separation axis r. Those are now comparable to the results in [9] and are shown in figure 4.10.

The right part of this figure is to be compared as it shows respectively the sum of all chromoelectric and chromomagnetic field components. This is in contradiction to the results from [9] where in the middle between quark and antiquark E^2 is positive while in our work it is negative compared to the vacuum. Also the magnetic field strength

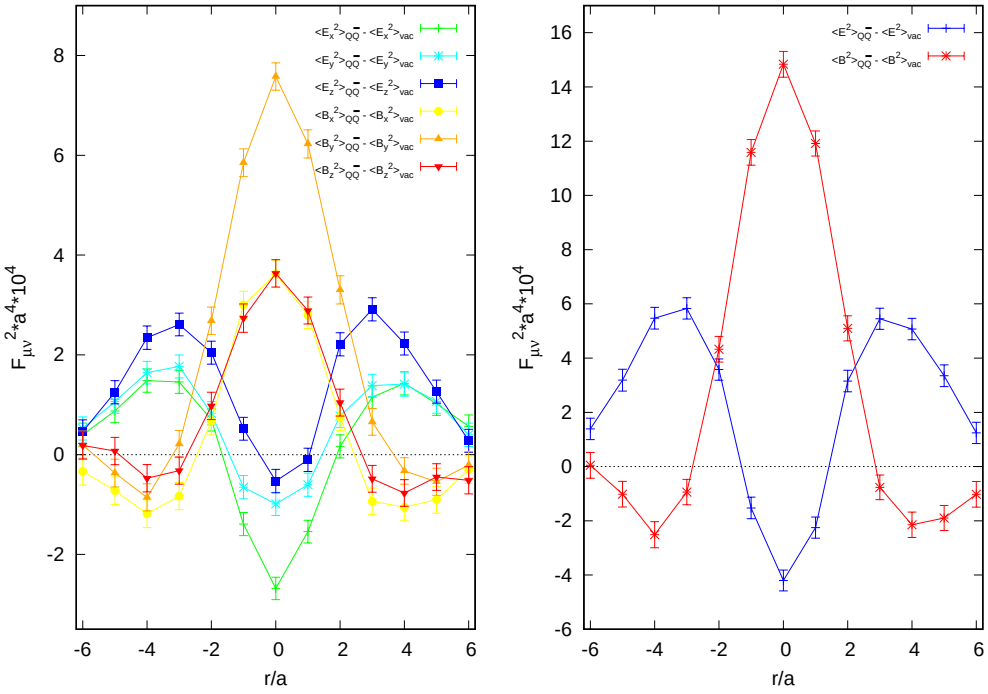

Figure 4.10: left: Colour field components of hybrid static potential Π_u on any axis perpendicular to the separation axis in the middle between quark and antiquark (mediator plane).
right: The sum of all components.

remains negative in euclidean space in [9] whereas in our results it is significantly positive compared to the vacuum.

In conclusion there is a large discrepancy between both results that cannot be explained by the different sets of quantum numbers chosen to compute the field strength. While in [9] the structure of the hybrid potential flux tubes for Π_u is very similar to the ordinary static potential, in our results excited gluons result in a significant rise of chromomagnetic field strength in between quark and antiquark suppressing the chromoelectric part of the flux tube there.

5 Conclusion

5.1 Summary

We computed the square of the chromoelectric and chromomagnetic field strength components for an ordinary and an example of hybrid static potential. This was done by considering a trial state in form of the ordinary Wilson loop first, followed by a modified Wilson loop with insertions according to the hybrid quantum numbers of Π_u. The convergence of those states was studied, investigating behaviour for different temporal separations of the Wilson loop. Additionally the entire 2D-plane along the insertions and the separation axis was covered, granting a complete picture of the gluonic distribution for this hybrid static potential. The results for the ordinary static potential were in agreement with literature ([7]). In the end our results for the hybrid state were compared to recent publications in [9] which led to high discrepancies whose origin still needs to be determined.

Investigating the structure of hybrid static potential flux tubes of a state with angular momentum $|L|= 1$ one finds significant differences to ordinary flux tubes. There are clear indications of local gluonic excitation in the middle between quark and antiquark causing those quantum numbers. This manifests in a large chromomagnetic field strength suppressing the chromoelectric field. There still remains a similar structure of positive chromoelectric field and negative chromomagnetic field compared to the vacuum connecting quark and antiquark. It is forced to adapt to the excitation in the middle though, resulting in a circular-like shaped gluonic distribution around the maximum in chromomagnetic field strength in the middle.

5.2 Outlook

Firstly the origin of the different results compared to [9] needs to be resolved. The single most important next step is to examine hybrid static potential flux tubes of other quantum numbers since at the moment there is no way to differentiate between effects characteristic for hybrid states in general and effects characteristic for this very state. It will be important to consider different separations of quark and antiquark. We also need to increase statistics to confirm the convergence of the state since errors for higher values of T are still too large.

Bibliography

[1] C. Morningstar, K. J. Juge, and J. Kuti; *Gluon excitations of the static quark potential*, In Quark confinement and the hadron spectrum III. Proceedings, 3rd International Conference, Newport News, USA, June 7-12, 1998, pages 179–182, 1998, hep-lat/9809015.

[2] Philipp Wolf, Marc Wagner; *Lattice study of hybrid static potentials*, arXiv:1410.7578 [hep-lat], 28.10.2014

[3] Christian Reisinger; *Hybrid static potentials in su(3) gauge theory on the lattice*, Master's thesis, Institut für Theoretische Physik, Goethe-Universität Frankfurt am Main, 03.2017

[4] C. Reisinger, S. Capitani, O. Philipsen, M. Wagner; *Computation of hybrid static potentials in SU(3) lattice gauge theory*, arXiv:1708.05562 [hep-lat], 18.08.2017

[5] A. Di Giacomo, M. Maggiore and S. Olejnik, Nucl. Phys. B 347, 441 (1990). doi:10.1016/0550-3213(90)90567-W

[6] Charlotte Meyerdierks; *Investigation of the structure of static potential flux tubes*, Bachelor's thesis, Institut für Theoretische Physik, Goethe-Universität Frankfurt am Main, 21.09.2017

[7] N. Cardoso, M. Cardoso, P. Bicudo; *Inside the SU(3) quark-antiquark QCD flux tube: screening versus quantum widening*, arXiv:1302.3633 [hep-lat], 14.02.2013

[8] M. Cardoso, N. Cardoso, P. Bicudo; *Lattice QCD computation of the gluon fields for the static hybrid quark-gluon-antiquark system, and microscopic study of the Casimir scaling*, arXiv:0912.3181 [hep-lat] 16.12.2009

[9] Pedro Bicudo, Marco Cardoso, Nuno Cardoso; *Colour fields of the quark-antiquark excited flux tube*, arXiv:1803.04569 [hep-lat], 12.03.2018

[10] Heinz J. Rothe, *Lattice gauge theories: an introduction*, New Jersey [u.a.] : World Scientific Publ., 3rd edition, 2006

[11] http://www.physics.utah.edu/%7Edetar/phycs6730/handouts/jackknife/jackknife/, date: 31.08.2017

[12] M. Wagner. Lattice SU(2) program. unpublished.